In-flight temperature of solid micrometric powders during cold spray additive manufacturing

Rija Nirina Raoelison, Mohamed Rabie Guéchi, Essolé Padayodi

In-flight temperature of solid micrometric powders during cold spray additive manufacturing.

Rija Nirina Raoelison[*1], Mohamed Rabi Guechi[1], Essolé Padayodi[2]

[1] Université de Bourgogne Franche-Comté - UTBM, Laboratoire Interdisciplinaire Carnot de Bourgogne, UMR 6303 CNRS, 90100 Belfort, France

[2] University of Bourgogne Franche-Comté - UTBM, ELLIADD, Pôle ERCOS, 90010 Belfort, France.

[*] corresponding author: rija-nirina.raoelison@utbm.fr (+33 3 84 58 30 97)

Abstract:

During cold dynamic gas spray additive manufacturing, the thermal field within particles is generally simplified by a state of an instantaneous uniform distribution over the particle's media at any position inside and outside the De-Laval nozzle. This paper addresses critical discussions using analytical and computational analysis of the transient heat transfer within the solid particles due to the convective exchange with the flowing gas. An analytical criterion depicts conditions of instantaneous uniform temperature over the range of typical cold spray data including various particle thermal conductivity, particle size range, dragging velocities, gas nature and gas setting conditions. The analytical depiction draws the conclusion that, during cold spraying, the temperature field within particles is mostly instantaneously uniform. The notion of instantaneousness is further investigated via computational analysis of the transient thermal gradient regimes within particles. The phenomenological computations enable for characterizing the duration of the transient stage prior to the state of uniform temperature. Comparisons with analytical particle's residence time using various scales of travelled distance give a more relevant notion of instantaneousness. The particle temperature is not strictly instantaneously uniform. However, such instantaneousness prevails for a covered distance unit of 1mm which is widely enacted in the literature to compute the particles temperature during cold spraying. As conclusive remarks, issues due to this instantaneousness of the particle temperature are reviewed and suitable alternatives for efficiently heating the particles during cold spraying are reported.

Keywords: cold spraying; thermal instantaneousness; parietal convection; uniform temperature; analytical criterion; CFD analysis.

Nomenclature

Latin-script symbol		
A, B, K	Constant	(-)
Bi	Biot Number	(-)
C	Heat capacity	($J.kg^{-1}.K^{-1}$)
C_D	Drag coefficient of particle	(-)
D	Diameter	(m)
F_D	Drag force	($kg.m.s^{-2}$)
Fo	Fourier number	(-)
h	Heat transfer coefficient	($W.m^{-2}K^{-1}$)
m	Mass	(kg)
M	Mach number	(-)
Nu	Nusselt number	(-)
P	Pressure	(Bar)
Pr	Prandtl number	(-)
r	Radial coordinate of the particle	(m)
Rs	Specific gas constant	($J.kg^{-1}.K^{-1}$)
RUT_p	Dimensionless ratio for a uniform particle temperature	(-)
t	Time variable	(s)
t_r	Particle residence time	(s)
t_U	Duration before the onset of a quasi-uniform temperature	(s)
T	Temperature	(K)
V	Velocity	($m.s^{-1}$)
V_r	Relative Velocity	($m.s^{-1}$)
x	Coordinate variable	(m)
X	Position	(m)
W	Lambert's function	(-)
W_{-1}	Branch of the Lambert's function	(-)
Greek-script symbol		
α	Thermal diffusivity	($m^2.s^{-1}$)
γ	Ratio of specific heat	(-)
δx	Distance	(m)
ζ	Eigenvalue	(-)
Ψ	Nozzle radius along the nozzle axis	(m)
Ψ^*	Radius of the nozzle throat	(m)
λ	Thermal conductivity	($W.m^{-1}.K^{-1}$)
μ	Dynamic viscosity	($kg.m^{-1}.s^{-1}$)
ξ	Intermediate variable	(m^{-1})
ρ	Density	($kg.m^{-3}$)
Δ	Differential	(-)
Subscript symbol		
c	Reference denoting centre of sphere	
cr	Reference denoting critical value	
g	Refers to gas	
gi	Reference denoting input conditions for the gas parameters	
min	Reference denoting minimum value	
p	Refers to particle	
0	Reference denoting an initial condition	
∞	Reference denoting a boundary condition	

1. Introduction

Among emerging additive manufacturing (AM) techniques, cold gas dynamic spraying (CGDS) is a recent variant that produces a solid-state and self-cohesion of micron and submicron particles using a high-speed collision generated by a supersonic gas flow at low temperature. Such a principle allows innovative possibilities that extend the suitability of thermal spray AM towards modern challenges including both technological and ecological aspects [1–4]. Various capabilities and technological solutions from CGDS have been demonstrated thanks to diversified achievements such as high productivity, safe use, flexibility in terms of materials, free forming, surface functionalization, better materials, restoration/repair and innovative painting using metallic powders, or further opportunities [1,3,4]. CGDS products can be a bulk component (of some millimetres in size) or ultrathin coatings (of a few nanometres in thickness) that can be heterogeneous or homogeneous in terms of material constituents or architecture for various applications [2].

Two major stages describe the behaviour of the CGDS process: (1) a fluid/solid interaction between particles and a gas flow, and (2) a high-speed collision of the particles onto a target (moving or motionless). This collision enables for creating the AM deposit. The kinematics of particles and the thermal exchange with the flowing gas govern these stages. Thus, both velocity and temperature of the particles, denoted (V_p, T_p), are major in-flight parameters for the particles. The literature of CGDS provides significant knowledges about V_p including suitable conditions for a successful deposition. For various metals, critical V_p values and reliable experimental measures are available [5–7]. The supersonic flow generated by the gas expansion enables to reach high V_p but can also suffers from low deposition efficiency due to kinematic limitation, particularly for low pressure cold spraying. Then, the in-flight temperature of the particles becomes another investigated parameter to enhance the deposition capability. Empirical models have shown that V_p also depends on the value of T_p prior to the collision. An increase in T_p promotes an adhesion due to thermomechanical softening [8–11], better ductility that increases bonded surface [5,8], or better oxide removal (over the particle's surface) produced by more deformation capability [11]. Generally, the critical V_p for adhesion decreases as T_p increases according to various empirical models which use a generic law depends on the term $\sqrt{1 - T_p/T_{melting}}$ [5,6,8].

A major task of CDGS users is therefore to identify the process conditions to reach the critical V_p of the material they work with. Experimental procedure as well as numerical simulation is suitable for that purpose. For micron powders used in CGDS, there are predictive kinematic models of the gas/particle interaction, analytical solutions of particle kinematics or reliable experimental measurements of V_p using viable laser system such as DPV2000 laser, Laser-2-Focus (L2F), or Particle Image Velocimetry (PIV) [12–14]. Thereby, considerable efforts have been made to characterize V_p, whereas T_p is less investigated. Due to the size of successful CGDS powders, less than 100µm [15], a reliable experimental characterization of T_p is difficult. The literature of CGDS rather apprehends T_p via numerical simulation that considers the particles as discrete phase under the following assumptions: a uniform distribution of T_p within particles, a convective heat transfer due to the gas using a Newton's law of cooling, and an advective transport of T_p that accounts for the motion of the particle dragged by the gas flow. This computation assumes that, instantaneously, T_p is homogeneous at any coordinates along the nozzle. Then, the variation of T_p does not depend on time but on the position of the particle along the nozzle. Due to the micrometric size of the particles used in cold spraying, such circumstance has been widely enacted but the issue of non-uniformity of T_p remains a matter of discussion. Katanoda studied the heat conduction within particles subjected

to a convection that is governed by a convective heat transfer assessed from the computation of gas flow throughout the nozzle [16]. Results of steady state analysis show that the assumption of uniform temperature may become untrue for low thermal conductive powders [16]. A further investigation is suggested in this paper that also aims to find out a selection criterion capable for predicting the situations of uniform temperature for CGDS powders. Conditions of uniform T_p are depicted using analytical laws and CFD simulations. To discuss the instantaneousness of the temperature uniformity, the transient thermal field of particles with respect to their residence time is also analysed. The depiction provided in this study uses baseline parameters of CGDS including typical gas flow parameters and powder features.

2. Computational models and data

2.1 Analytical parietal heat transfer and solution

The equations (Eq.1) and (Eq. 2) present the analytical formulation of the heat transfer within particles due to the thermal interaction with the flowing gas during cold spraying. The convective parietal heat transfer is modelled by a third kind boundary condition, that is a heat flux continuity across the particle solid/fluid interface defined by the Newton's law of cooling. Albeit simple, this problem has an attractive analytical solution that enables for characterizing the particles temperature in CGDS. Assuming a homogeneous initial temperature (Eq. 3) and a radial heat conduction, the spatial-temporal variation of the particle's temperature is a function series which can be reduced into a single term, in a usable form for identifying conditions of uniform distribution. It provides a formula of time dependant inner distribution of T_p (Eq. 4). The analytical details for solving (Eq. 1-3) are provided in appendix A.

$$\frac{1}{r^2}\frac{d}{dr}\left[\lambda_p r^2 \frac{dT_p(r,t)}{dr}\right] = \rho_p C_{pp} \frac{dT_p(r,t)}{dt} \qquad for \begin{cases} r \in \left[0, \frac{D_p}{2}\right] \\ t \geq 0 \end{cases} \tag{Eq. 1}$$

$$-\lambda_p \left.\frac{dT_p(r,t)}{dr}\right|_{r=\frac{D_p}{2}} = h\left[T_p\left(\frac{D_p}{2}, t\right) - T_\infty\right] \tag{Eq.2}$$

$$T_p(r,0) = T_0 \tag{Eq. 3}$$

$$T_p(r,t) = (T_0 - T_\infty)\left[2\frac{sin\zeta - \zeta cos\zeta}{\zeta - sin\zeta cos\zeta} e^{-\zeta^2 \frac{\lambda_p \quad 4}{\rho_p C_{pp} D_p^2} t} \frac{1}{\frac{2\zeta}{D_p} r} sin\left(\frac{2\zeta}{D_p} r\right)\right] + T_0 \tag{Eq. 4}$$

Where ζ is the first positive root of the equation:

$$\frac{\zeta}{\tan\zeta} = 1 - Bi \quad \text{with} \quad Bi = \frac{h\frac{D_p}{2}}{\lambda_p} \tag{Eq. 5}$$

2.2 Analytical formula of particle's residence time

The 2nd Newton's law of motion does define the time-dependent kinematics of particles in cold spraying. For spherical particles, (Eq. 6) specifies the time-dependent Lagrangian formulation of motion without interaction between particles. The major source of the particles motion is the drag force caused by the moving fluid (Eq. 7). Gravity effect is negligible since CGDS particles are small

enough to produce significant gravitational force. After some mathematical manipulations [17] and using properties of Lambert's function, the analytical solution for the residence time of particles is described by the equation (Eq. 8).

$$m_p \frac{dV_p}{dt} = F_D \quad \text{(Eq. 6)}$$

$$F_D = \frac{3}{4}\frac{\rho_g}{\rho_p}\frac{m_p}{D_p} C_D\left(V_g - V_p\right)\left|V_g - V_p\right| \quad \text{(Eq. 7)}$$

$$t_p = -\frac{4}{3}\frac{\rho_p}{\rho_g}\frac{D_p}{C_D}\left\{\frac{1}{V_g - V_{p0}} + \frac{1}{V_g} W\left[\frac{-V_g}{V_g - V_{p0}}\, e^{\frac{-V_g}{V_g - V_{p0}}}\, e^{-\frac{3\rho_g C_D}{4\rho_p D_p}dx}\right]\right\} \quad \text{(Eq .8)}$$

Where W denotes the W_1 branch of Lambert's function defined by the expressions (Eq. 9), (Eq. 10) and (Eq. 11) depending on the range of the variable x [18]. Note that in this study, the values of the computed variable x vary in between -1/e and 0.

$$\begin{cases} \text{For } -\frac{1}{e} \le x < -0.333, \\ W_{-1}(x) = -1 + p - \frac{1}{3}p^2 + \frac{11}{72}p^3 - \frac{43}{540}p^4 + \frac{769}{17280}p^5 - \frac{221}{8505}p^6 \\ with\ p = -\sqrt{2(ex+1)} \end{cases} \quad \text{(Eq. 9)}$$

$$\begin{cases} For\ -0.333 \le x \le -0.033, \\ W_{-1}(x) = \frac{-8.0960 + 391.0025x - 47.4252x^2 - 4877.6330x^3 - 5532.7760x^4}{1 - 82.9423x + 433.8688x^2 + 1515.3060x^3} \end{cases} \quad \text{(Eq. 10)}$$

$$\begin{cases} For -0.033 \le x < 0, \\ W_{-1}(x) = L_1 - L_2 + \frac{L_1}{L_2} + \frac{(-2+L_2)L_2}{2L_1^2} + \frac{(6-9L_2+2L_2^2)L_2}{6L_1^3} + \frac{(-12+36L_2-22L_2^2+3L_2^3)L_2}{12L_1^4} \\ \quad + \frac{(60-300L_2+350L_2^2-125L_2^3+12L_2^4)L_2}{60L_1^2} \\ with\ L_1 = ln(-x);\ L_2 = ln\left(-ln(-x)\right); \end{cases}$$

(Eq. 11)

Eq. 8 depends on gas density and gas velocity that can be determined from the isentropic gas flow model:

$$\rho_g = \frac{P_{gi}}{R_S T_{gi}}\left(1 + \frac{\gamma - 1}{2}M^2\right)^{\frac{-1}{\gamma-1}} \quad \text{(Eq. 12)}$$

$$V_g = M\gamma^{\frac{1}{2}}\left(1 + \frac{\gamma-1}{2}M^2\right)^{-\frac{1}{2}}\left(R_s T_{gi}\right)^{\frac{1}{2}} \quad \text{(Eq. 13)}$$

Where $P_{g\,i}$ and $T_{g\,i}$ are the gas input parameters. They are set as steady state initial conditions at the nozzle inlet. R_S is the specific gas constant and γ the heat specific ratio of the gas. The isentropic law through the convergent-divergent nozzle (Eq. 14) defines the values of the Mach number M for any nozzle radius (Ψ) depending on a throat radius (Ψ^*). These equations set involve major CGDS parameters that allow for a large depiction although these parameters are numerous and interrelated.

$$\left(\frac{\Psi}{\Psi^*}\right)^2 - \frac{1}{M}\left[\frac{2}{\gamma+1}\left(1+\frac{\gamma-1}{2}M^2\right)\right]^{\frac{\gamma+1}{2(\gamma-1)}} = 0 \qquad \text{(Eq. 14)}$$

2.3 Finite element model of the gas/particle parietal heat transfer

Additional investigations use a finite element simulation of the heat and mass transfer within the gas flow, the thermal interaction between gas and particle, and the time dependent conductive heat transfer within the particle. This is a phenomenological computation that relies on the Navier-Stokes equations for an incompressible flow and a Newtonian fluid; and on the enthalpy formulation for the energy conservation equation. The particle is motionless, then the interface between the particle domain and the fluid domain is a fixed wall. The thermal exchange across this interface is a continuity of both heat flux and temperature. Inside the particle, the transient heat conduction is described by the energy balance equation for solid media assuming no heat generation. The numerical simulations are performed using the COMSOL software and properties at standard room temperature for the particles (Table 1). For the gas, temperature dependent data are used [19].

	Al_2O_3	Ti	Al	Cu
ρ (kg/m^3)	3950	4510	2700	8900
C_p (J.kg^{-1}K^{-1})	795	520	897	382
λ (W.m^{-1}.K^{-1})	10	20	297	390

Table 1. Computational data for the particles.

The computational model requires to consider the nature of the flow over the particle. The flow regime can be described by the Reynolds number. A flow past a sphere was shown to be axisymmetric with a laminar regime for *Re* values lower than ~24, and then with a development of stationary rings for *Re* up to ~130 [20,21]. For ~130<Re<~300-400, since an onset of weak instable flow may occur at the downstream zone as discussed in the literature, a 3D computation prevails. [21,22]. For the computational data range in this study, the Reynolds number variance is depicted on Fig. 1. An axisymmetric flow generally prevails over the D_p range for the case He gas; and for low D_p alone in case of air gas. In this paper, we perform the computations with a 3D model. Fig. 2 describes the computational model that consists of a finite cylinder fluid domain and boundary conditions which reflect the conditions of flow surrounding the particle. The fluid domain has a diameter of 20*D_p and length of 40*D_p while D_p stands for particle diameter. The particle is placed on the axis of this cylinder fluid domain as specified on Fig. 2. This small-scale simulation is suitable to compute the parietal heat transfer over the particle surface due to the gas flow. The change in gas density is insignificant within such a very short distance as compared to the variation through the nozzle governed by both compression and expansion of the propellant gas. Therefore, a compressible flow no longer prevails at such a small scale. The parietal flow surrounding CGDS particles is thereby nearly incompressible. Local characteristics of the gas in terms of temperature, velocity and pressure, denoted $(T_\infty, V_\infty, P_\infty)$, at particle's position are considered to define the local state of the gas. The values of $(T_\infty, V_\infty, P_\infty)$ are assumed to be initially uniform within the fluid domain while the particle is assigned an initial temperature T_0 of 20°C. The set (T_∞, V_∞) is also used as inlet condition for the gas flow where V_∞ is the gas velocity relative to the particle velocity $(V_\infty = V_g - V_p)$. At the opposite edge of the inlet edge, the outlet flow is defined by a free flow. At the lateral boundary of the fluid domain, a temperature condition (T_∞) is prescribed and the flow is parallel to this boundary. These conditions are specified on Fig. 2. The model is discretized with an element size of 0.1xD_p using 3D linear tetrahedral elements. The mesh is then characterized by typical numbers of about 2 500 000, 450 000 and 2 100 000 for the elements, the nodes and the degrees of freedoms, respectively.

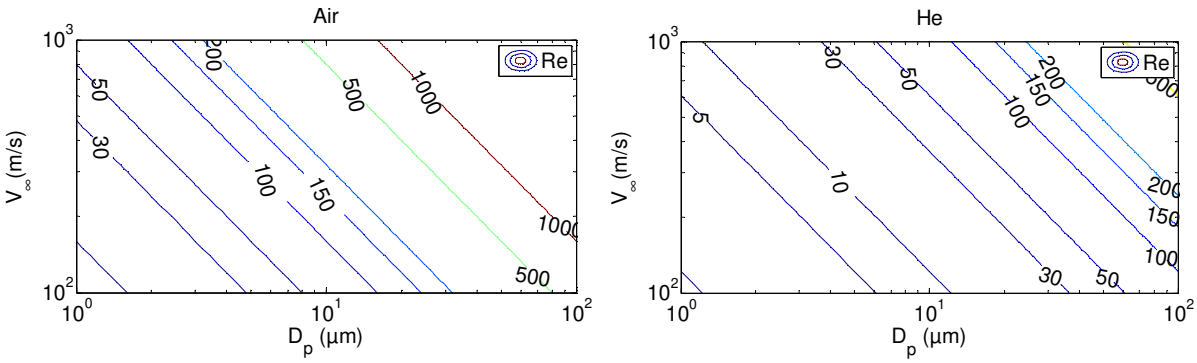

Fig. 1. Reynolds number values for the computational data range.

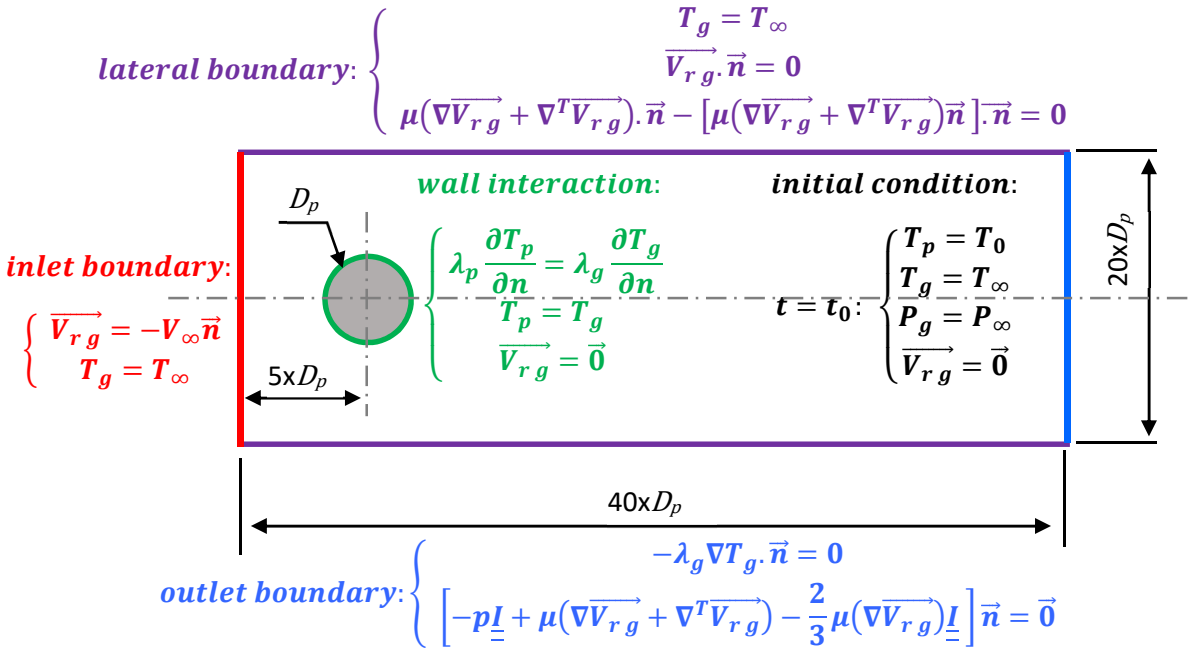

Fig. 2. Cross-section of the 3D computational model considering the fluid domain as a finite cylinder domain, and the particle domain as a sphere placed on the axis of this cylinder fluid domain.

This model is applied to an experimental case available in the literature which used the data specified in Table 2. This is a forced-air cooling experiment over a sphere with a measurement the transient temperature at the centre of this sphere [23]. The computational model reproduces the experimental measurement with a good accuracy. The comparison between the numerical simulation and the literature data shows an error less than 10% (Fig. 3). Note that the numerical data of (Fig. 3). Note that the numerical data of (Fig. 3) are available as appendix data (tables A3, A4). This agreement supports the predictive capability of the computational model and its suitability for investigating the parietal thermal exchange over a spherical media due to a forced convection as considered in this paper.

V_∞(m/s)	T_∞(°C)	T_0(°C)	ρ (kg/m^3)	C_p (J.kg^{-1}K^{-1})	λ (W.m^{-1}.K^{-1})
1.5	4	22	1076	3666	0.53

Table 2. Data and properties of the sphere used in [23] for a forced-air cooling experiment with a measurement of the temperature at the centre of this sphere.

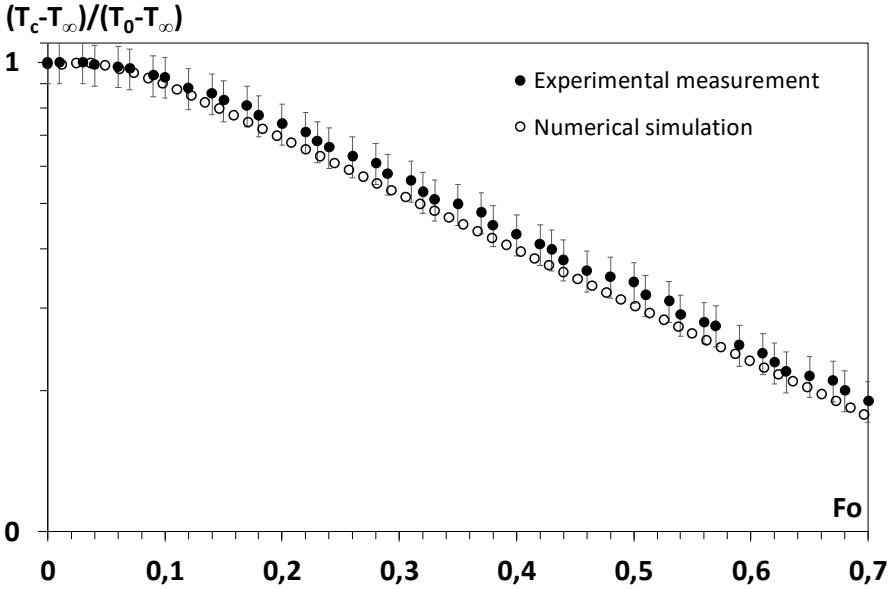

Fig. 3. Numerical simulation of the experimental case in [23], and comparison with the experimental measurements that shows the predictive capability of the computational model. An error of 10% is added to the experimental data provided in [23].

3. Results and discussions

3.1 Circumstance of a uniform T_p using an analytical depiction

(Eq. 3) gives a basic expression of uniform T_p using the equality $T_p\left(D_p/2, t\right) = T_p(0, t)$ that results in the following generic condition:

$$\frac{sin(\zeta)}{\zeta} = 1 \qquad \text{(Eq. 15)}$$

Both Eq. 5 and Eq. 15 give a root that corresponds to a Biot number of 10^{-3} for which the criterion Eq. 15 does not strictly equal to 1 but to 0.999, that is nearly 1. Such Biot number value is low enough to state a case of uniform temperature and becomes unsuitable to discuss the event of non-uniform T_p. Eq. 5 and Eq. 15 can be satisfied by other roots with an uncertainty less than 10% for the criterion Eq. 15. Those roots give a range $10^{-3} \leq$ Bi ≤ 0.2 with an accuracy range of $0.999 \leq sin(\zeta)/\zeta \leq 0.906$. Then, assuming $sin(\zeta)/\zeta = 0.906$ is an accurate lower bound for Eq.15, the eigenvalues ζ of (Eq. 4) for $Bi \lesssim 0.2$ satisfy this criterion (Eq. 15). Considering a critical value $Bi_{cr} = 0.2$, a condition $(Bi \lesssim Bi_{cr})$ enables for finding a criterion that can correlate several variables such as kinematic variables, particle size, and thermophysical properties of both gas and particle.

Bi is correlated to Nusselt number via the heat transfer coefficient:

$$Nu = 2\frac{\lambda_g}{\lambda_p}Bi \qquad \text{(Eq. 16)}$$

Using the Ranz-Marshall correlation and the Reynolds number expression depending on V_∞, we can find out the following result:

$$\frac{V_\infty D_p}{2} = 0.55\frac{\nu}{Pr^{\frac{2}{3}}}\left(\frac{\lambda_p}{\lambda_g}Bi - 1\right)^2 \simeq \frac{1}{2}\frac{\nu}{Pr^{\frac{2}{3}}}\left(\frac{\lambda_p}{\lambda_g}Bi - 1\right)^2 \qquad \text{(Eq. 17)}$$

Thus, the criterion ($Bi \lesssim Bi_{cr}$) for a uniform T_p can be expressed in terms of $V_\infty D_p$ and properties ratio as follows:

$$RUT_p = \frac{V_\infty D_p}{\frac{\nu}{Pr^{\frac{2}{3}}}\left(\frac{\lambda_p}{\lambda_g}Bi_{cr}-1\right)^2} \lesssim 1 \qquad \text{(Eq.18)}$$

The relationship (Eq. 18) defines an analytical condition where the left term, denoted RUT_p (ratio for uniform T_p) in this paper, accounts for the effect of the gas flow over the particle's surface via V_∞, and the effect heat conduction within particles via D_p and λ_p. Fig. 4 computes isovalues of RUT_p depending on $V_\infty D_p$ and λ_p, in case of air (Fig. 4a) and helium (Fig. 4b). The computational data for λ_p cover a large spectrum of CGDS materials, from less to more conductive powders, from alumina to copper typically (~10-400Wm^{-1}K^{-1}). The computational range for $V_\infty D_p$ also covers typical cold spray data, viz D_p of 1-100µm [15] and Mach number range of 1.5-3 for which V_∞ is about 100-700m/s for air and 400-2000m/s for helium. The isentropic equations combined with the analytical expression of particle kinematics enable for determining such a range of V_∞, depicted using variance of both particles feature $\rho_p D_p$ and Mach number M (appendix D). Data collected from a literature survey are also used for $\rho_p D_p$ [15]. Note that the computational range of M corresponds to a variation of nozzle expansion ratio reported in the literature [15]. Together, these ranges provide representative data to compute the ratio RUT_p.

RUT_p for air (Fig. 4a) falls below one, except for both low conductive materials (~10Wm^{-1}K^{-1}) and high $V_\infty D_p$ values (~0.1). Such combination would not meet the situation of uniform temperature. RUT_p for helium shows similar tendency, but the zone of non-uniform temperature (RUT_p >1) is slightly broader. Since the thermal conductivity of helium is higher than that for air, the thermal exchange with particles is more efficient for air than for helium. Other things equal, helium thus produces a less efficient particle heating. A low conductive particle subjected to such inefficient heating promotes a circumstance of non-uniform T_p, as shows the comparison of RUT_p between air and helium. However, for thermally conductive materials such as metals that are widely used in cold spraying, uniform T_p prevails. The condition RUT_p <1 covers the range of metals thermal conductivities over the range of computed $V_\infty D_p$ (Fig. 2).

Typical experimental working zones depending on $V_\infty D_p$ are presented in Fig. 5 for the representative CGDS materials. Fig. 5a corresponds to the case of typical low D_p. The condition RUT_p <1 is satisfied for this case, that stands for an occurrence of instantaneous uniform temperature. Regarding the typical high D_p (Fig. 5b), the criterion RUT_p <1 also covers the spectrum of pragmatic CGDS materials, except in case of alumina powders combined with the use of helium as propellant gas. Uniform T_p does not prevail for this case since the low thermal conductivity of alumina and the high thermal conductivity of helium involves less efficient particle heating as previously discussed.

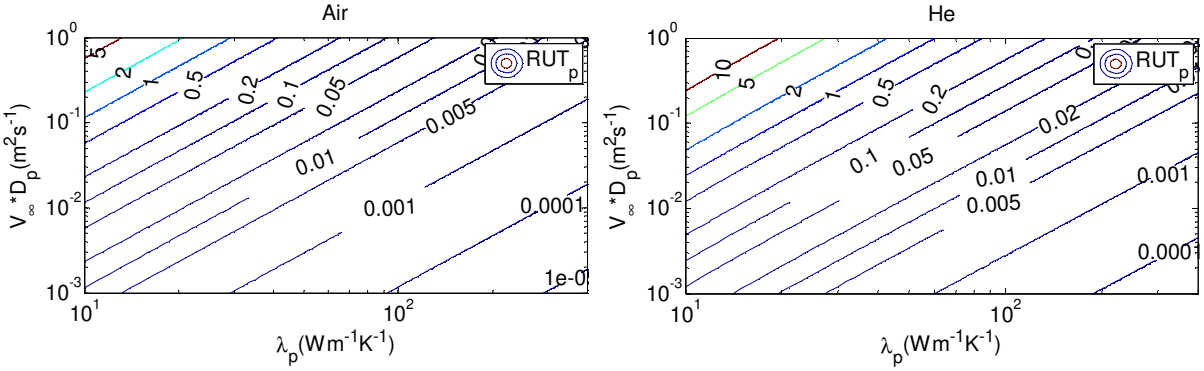

Fig. 4. Isovalues of RUT_p depending on $V_\infty D_p$ and λ_p, in case of Air (a) and He (b).

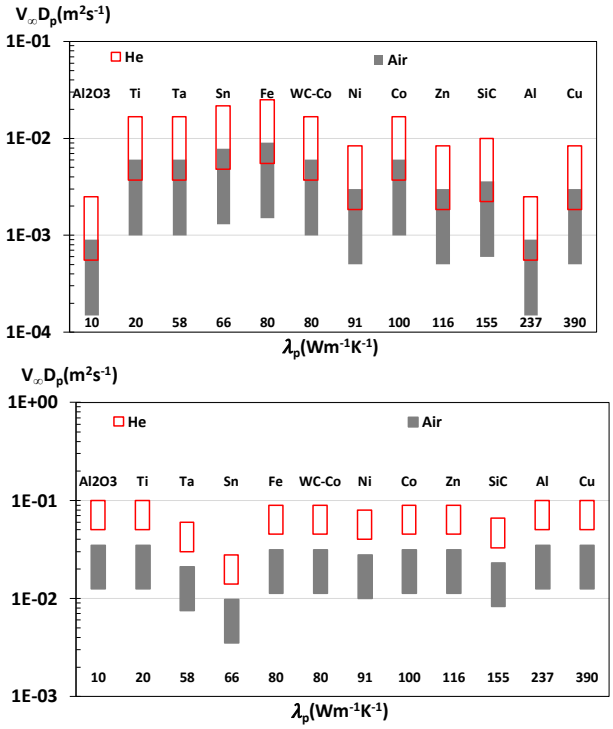

(a) (b)

Fig. 5. Computational range for $V_\infty D_p$ using typical cold spray D_p from [15] and typical computed V_∞ of about 100-700m/s for Air and 400-2000m/s for He. (a) case of low D_p, (b) case of high D_p.

These results suggest that during cold spraying, the temperature field within particles is mostly instantaneously uniform. This consideration is generally enacted in the literature of cold spraying for the smallness of particles size. Cold spray particles are small enough to have enough thermal inertia. The rate of variation in energy produced by both particle's density and heat capacity is too weak to cause a significant self-heating, and then a change in temperature. Thus, the thermal variation within particles is mainly due to the heat conduction governed by a fast-thermal gradient which evolves towards a uniform temperature distribution because of the heat diffusion through a very short distance such as the particle's radius. However, the instantaneousness of this uniform distribution remains a subjective concept without any quantitative notion in terms of reference time. In the literature for cold spraying, there is no temporal reference for this instantaneousness which is simplified into a thermal state of the particle at its location within the gas flow. Such statement makes the notion of instantaneousness insufficient for a clear determination of the particles in-flight temperature. The next section investigates the notion of instantaneousness using the particle's residence time as characteristic reference time. This residence time is determined using the analytical expression of section 2.2.

3.2 Notion and suitability of an instantaneously uniform T_p

The travel duration of a particle over a small distance, denoted dx, is a reference time that can characterize the instantaneousness of the temperature homogenization within the particle while the parietal convection of the fluid over the particle surface occurs during this travel duration, denoted particle residence time or t_p in this study. The analytical law of the residence time is depicted using two major variables: the term $\rho_p D_p$ and the Mach number M. Typical range of the literature is used

for $\rho_p D_p$ (Fig. 6). We remind that the values of M computed by the isentropic expansion law define the variation of both density and velocity of the gas, the inlet pressure P_{gi} and the inlet temperature T_{gi}. In the literature, representative experimental ranges of (P_{gi}, T_{gi}) are (10Bar, 20°C) and (40Bar, 800°C) for air; and (10Bar, 20°C) and (35Bar, 600°C) for helium [2].

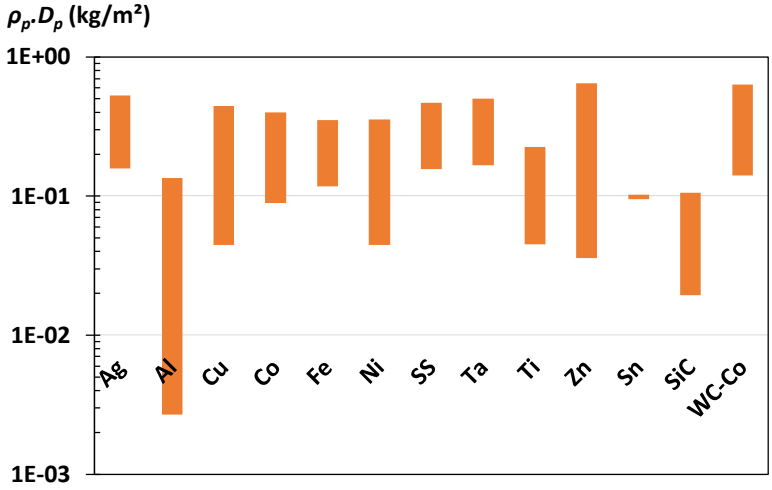

Fig. 6. Typical $\rho_p D_p$ values in cold spraying.

Results of t_p are plotted for the following covered distances: 1µm (Fig. 7), 10µm (Fig. 8), 100µm (Fig. 9) and 1mm (Fig. 10). Note that δx =1mm is the reference length unit of the literature to compute the variation of t_p along the nozzle axis. These sub-millimetres values of δx are adopted to include more small length unit so that shorter scale ranges comparable to the particle size are considered. Basically, t_p lasts some nanoseconds or some microseconds depending on δx. Such length of time can be compared with the duration of the transient heat transfer within particles (t_U) prior to the occurrence of a quasi-uniform temperature. The computations of t_U rely on appropriate circumstances that do involve heterogeneous thermal field so that the stage before the occurrence of uniform temperature distribution is maximized. A large initial gap between particle temperature and gas temperature is conducive to such conditions that are better satisfied with the gas setting of (40Bar, 800°C) for air and (35Bar, 600°C) for helium. Then, input values of T_∞ are set to 600°C and 800°C for air and helium respectively. The computational values of V_∞ rely on typical gas velocities depicted by the isentropic law (Fig. 11). Table 3 summarizes these boundary conditions for each computational case.

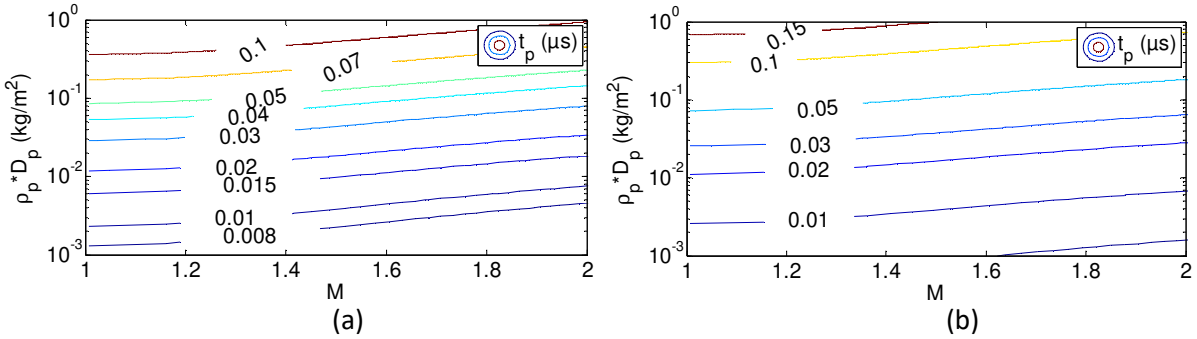

Fig. 7. Analytical depiction of particle residence time for $\delta x = 1\mu m$, (a): Air, P_{gi}=40Bar, T_{gi}=800°C; (b): He, P_{gi}=35Bar, T_{gi}=600°C.

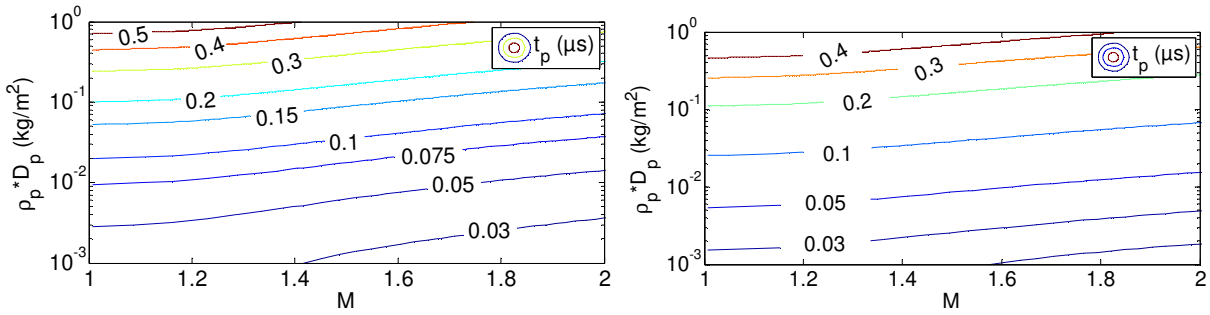

Fig. 8. Analytical depiction of particle residence time for $\delta x = 10\mu m$, (a): Air, P_{gi}=40Bar, T_{gi}=800°C; (b): He, P_{gi}=35Bar, T_{gi}=600°C.

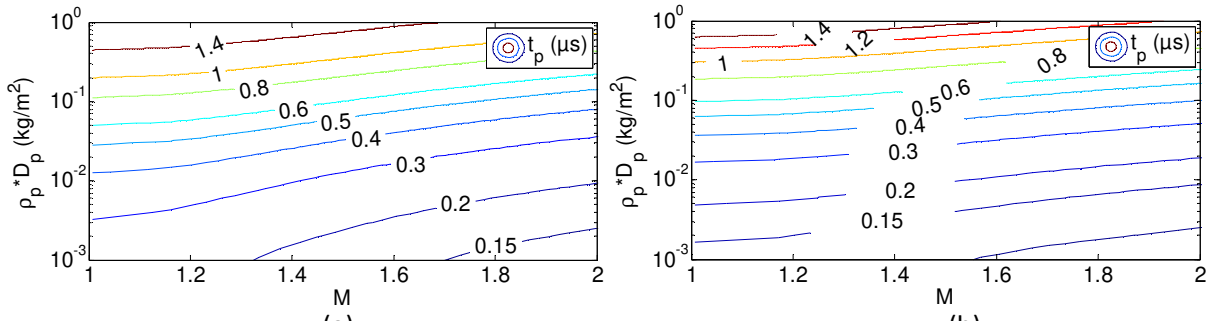

Fig. 9. Analytical depiction of particle residence time for $\delta x = 100\mu m$, (a): Air, P_{gi}=40Bar, T_{gi}=800°C; (b): He, P_{gi}=35Bar, T_{gi}=600°C.

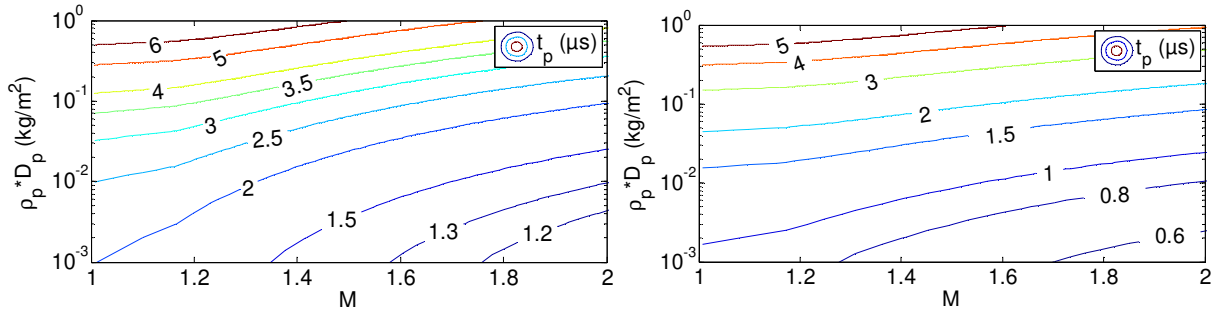

Fig. 10. Analytical depiction of particle residence time for $\delta x = 1mm$, (a): Air, P_{gi}=40Bar, T_{gi}=800°C; (b): He, P_{gi}=35Bar, T_{gi}=600°C.

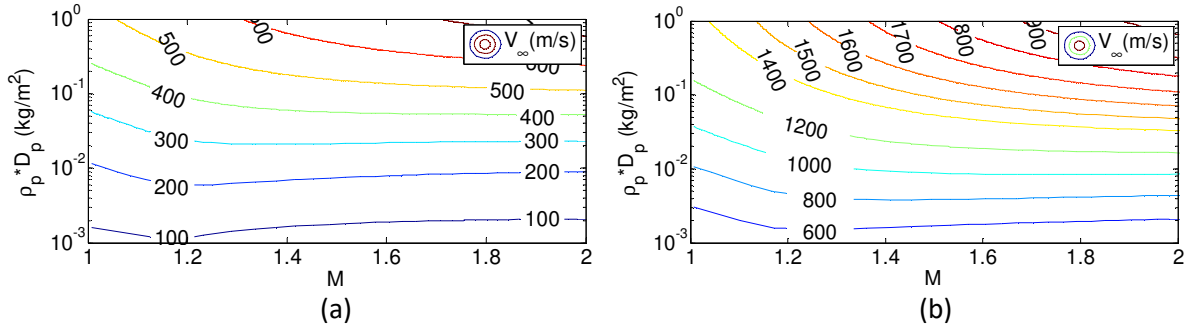

Fig. 11. Analytical depiction of the relative particle/gas velocity in cold spraying. (a): Air, P_{gi}=40Bar, T_{gi}=800°C; (b): He, P_{gi}=35Bar, T_{gi}=600°C.

	Cu				Al		
Gas	D_p(µm)	V_∞(m/s)	T_∞(°C)	Gas	D_p(µm)	V_∞(m/s)	T_∞(°C)
Air	5	300	800	Air	1	150	800
	50	600			50	300	
Helium	5	1200	600	Helium	1	800	600
	50	1800			50	1200	
	Ti				Al_2O_3		
Gas	D_p(µm)	V_∞(m/s)	T_∞(°C)	Gas	D_p(µm)	V_∞(m/s)	T_∞(°C)
Air	10	350	800	Air	1	150	800
	50	550			50	550	
Helium	10	1300	600	Helium	1	800	600
	50	1600			50	1600	

Table 3. Computational values of the boundary conditions T_∞ and V_∞.

Regarding the choice of powder nature, this study focuses on a few representative cases instead of considering each CGDS material that involves too many cases to compute. Representativeness in terms of both thermal conductivity and range of $\rho_p D_p$ is enacted for sake of consistency. Al_2O_3, Al and Cu are considered to represent less, intermediate and most thermally conductive powders. The computation includes also the case of Ti that has the lowest thermal conductivity among metals and is widely investigated in Cold Spraying. Together, these whole variables and materials cases involve 40 computational combinations.

Fig. 12 shows typical evolutions of the thermal gradient within the fluid and the particle computed by the CFD simulation. The flow direction is along the axis x of the reference system (x, y, z). The thermal field of particles begins by a radial distribution (Fig. 12a). The particle is continuously heated by the upstream flow, and consequently T_p decreases at the downstream zone. The thermal gradient within the particle follows this heating flow that sustains a decreasing temperature towards the flow direction (Fig. 12b). On the cross section normal to the flow direction, the thermal gradient within the particles remains radial (Fig. 12c). This collapsing thermal gradient along the direction x is a stable regime of T_p during the parietal heat exchange. Note that the temperature distribution within the particle is axisymmetric (Fig. 12c) due to the axisymmetric nature of flow until the stable thermal gradient regime (Fig. 12e, Fig. 12f).

The temperature discrepancy within the particle, we denote ΔT, progressively decreases towards a neglectable thermal gradient that also remains stable over the time as shown in Fig. 13 for each computed case. This regime of ΔT characterizes the duration of the transient time before the weak thermal gradient persists. ΔT converges to a weak value that specifies the duration (t_U) prior to a thermal quasi-uniformity within the particle. A highly conductive media combined with a very short conduction path, as represented by the cases of low D_p Al and Cu particles, produces a very fast transient thermal gradient since the uniform T_p readily occurs before 10^{-9}s (Fig. 13a, Fig. 13b). For the other heat conduction cases, t_U ranges in between 10^{-8}s and 10^{-5}s. The value of t_U is respectively reported in Tables 4 (Cu), Table 5 (Al), Table 6 (Ti), and Table 7 (Al_2O_3).

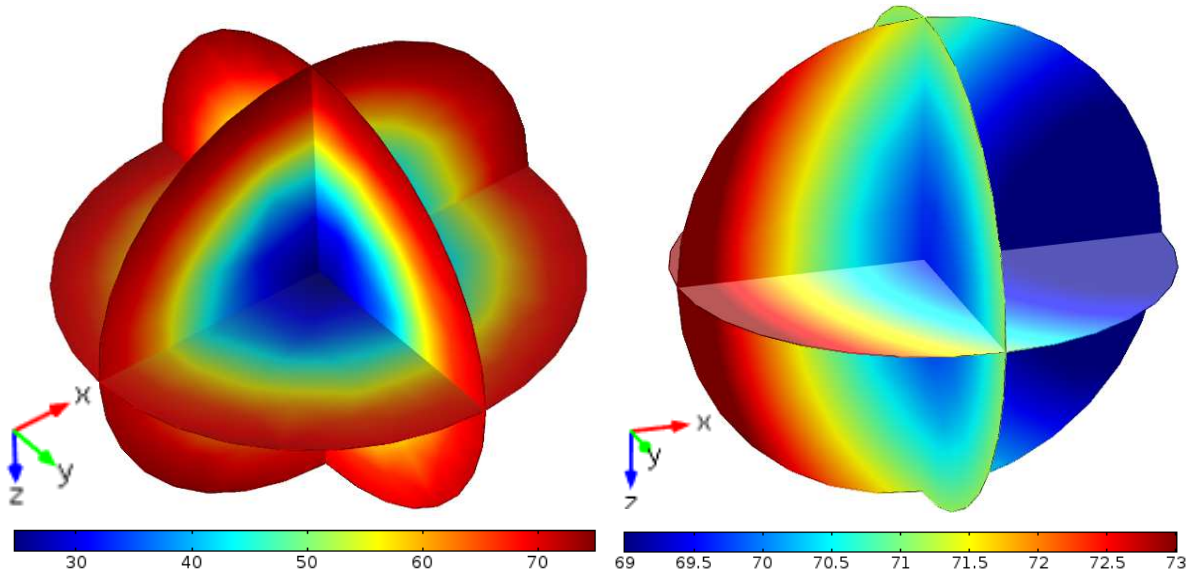
x
y
z
30
40
50
60
70
x
y
z
69
69.5
70
70.5
71
71.5
72
72.5
73

(a) (b)

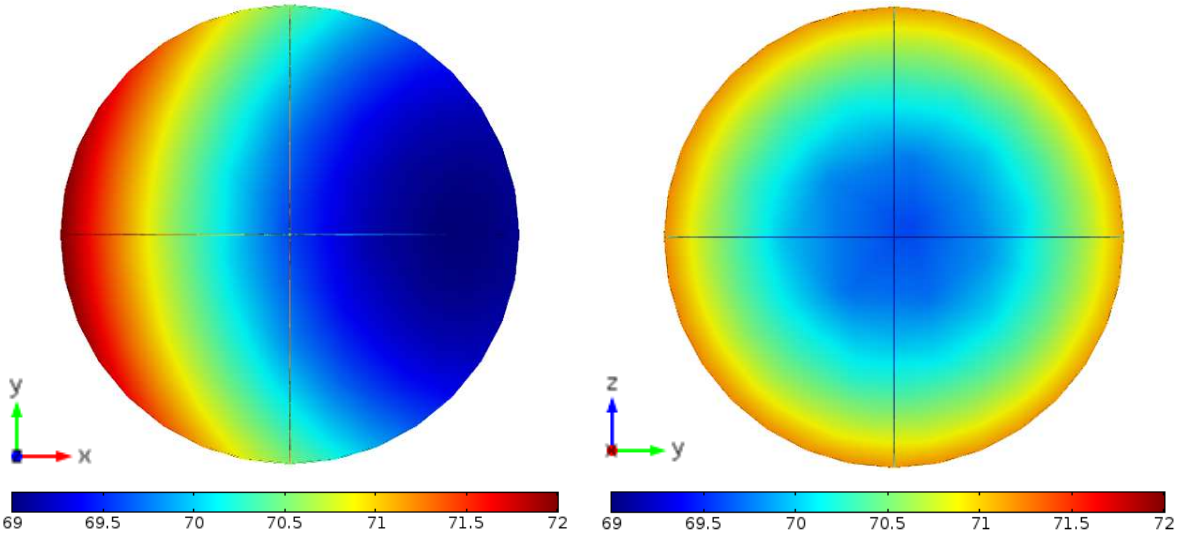
y
x
69
69.5
70
70.5
71
71.5
72
z
y
69
69.5
70
70.5
71
71.5
72

(c) (d)

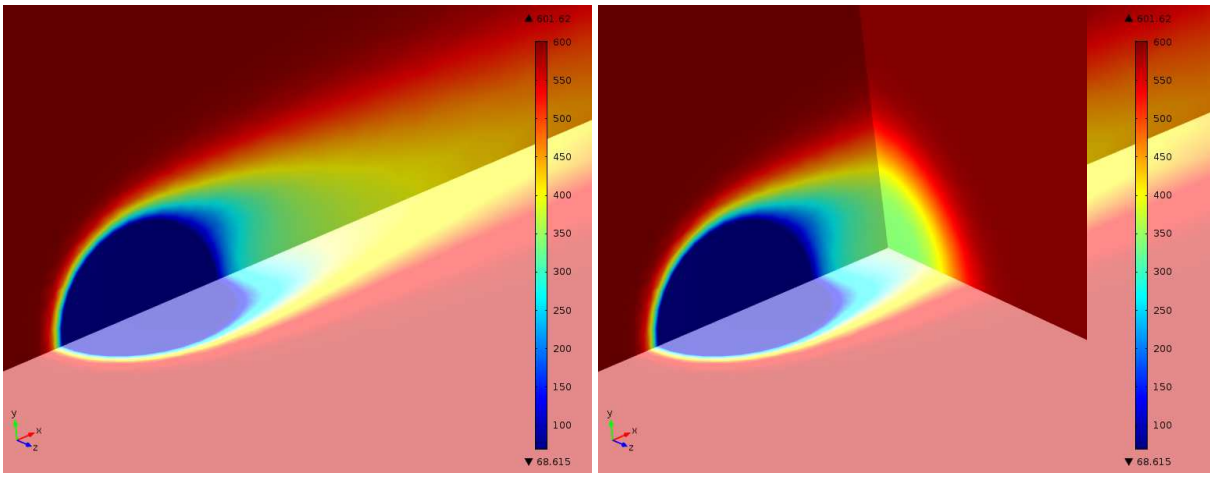
▲ 601.62
600
550
500
450
400
350
300
250
200
150
100
▼ 68.615
▲ 601.62
600
550
500
450
400
350
300
250
200
150
100
▼ 68.615

(e) (f)

Fig. 12. Typical progressions of the thermal field (°C) illustrated by the case Al (D_p=50µm, helium with V_∞=1200m/s and T_∞=600°C), that begins by a radial T_p (a) (t=5.10^{-7}s); towards a stable thermal gradient regime (b) (t=1.10^{-5}s) that decreases along the flow direction x (c) but remains radial on the plan normal to the direction x (d). Axisymmetric nature of the flow over the particle (t=1.10^{-5}s) revealed along x (e) and in the plan normal to x (f).

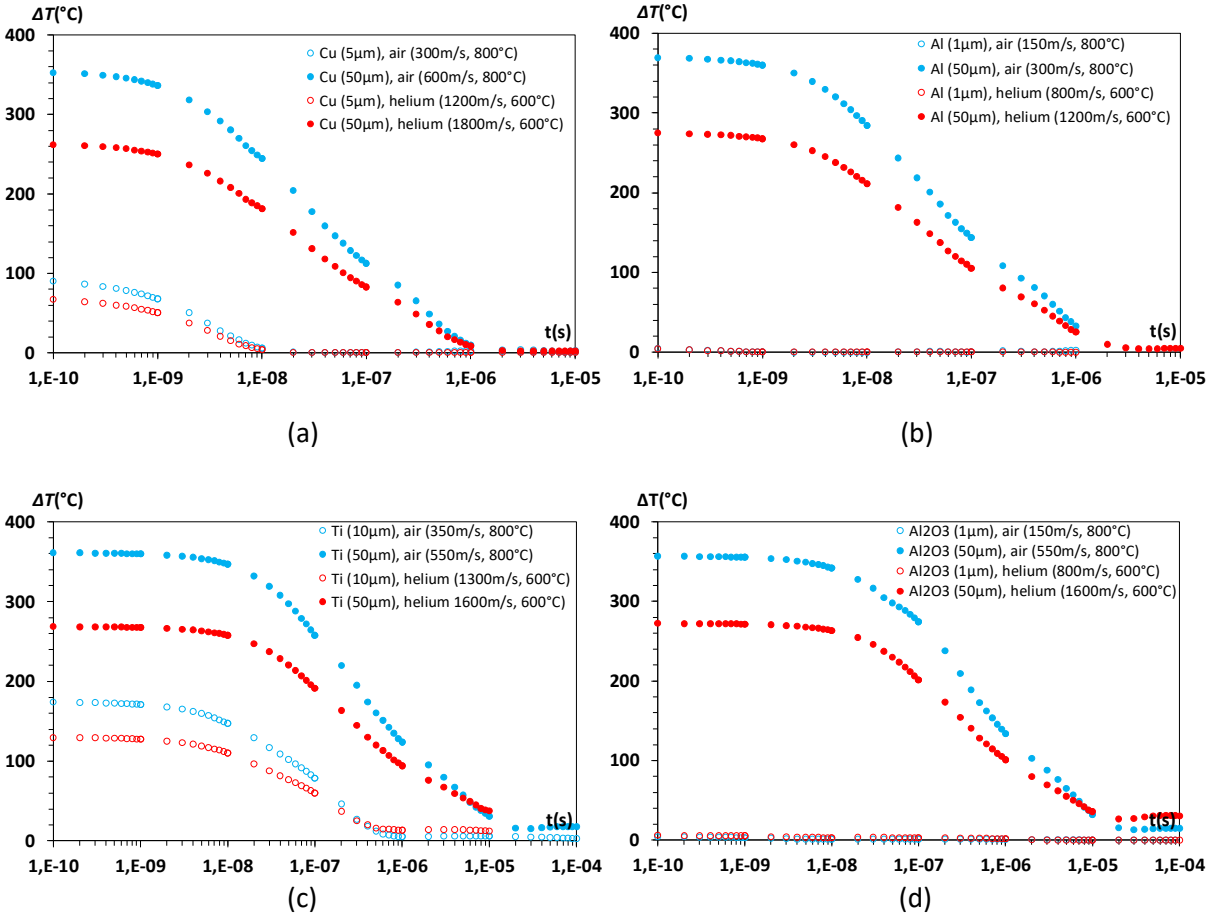

Fig. 13. Regime of ΔT towards a converged weak value that characterizes the duration (t_U) prior to a thermal quasi-uniformity within the particles. Case of copper particle (a), aluminium particle (b), titanium particle (c), and alumina particle (d).

.

The tables (Table 4-7) compare the thermal duration t_U to the analytical residence time t_p for each travelled distance δx. Since the good thermal conduction of Al and Cu eases a fast temperature homogenization, the strong thermal gradient within these particles quickly falls to low values to give a quasi-uniform T_p, for t_U in the range of 10^{-9}-10^{-6}s. The ratio t_p/t_U shows how instantaneously uniform is T_p. When $t_p > t_U$, the particle has produced uniform temperature before it has travelled the distance dx that corresponds to t_p. The reference distance $\delta x = 1mm$ of the literature is conducive to a uniform T_p and supports thereby the notion of instantaneous uniform temperature widely enacted using $\delta x = 1mm$. However, this instantaneousness notion becomes tricky if shorter dx is considered as unit reference. For δx of 1µm, 10µm, and 100µm, T_p is not strictly instantaneously uniform, particularly for a very short unit of travelled distance such as 1µm-100µm.

The particle residence time is less than the time of quasi-uniform T_p onset ($t_p/t_U < 1$). Then, short distances similar to CGDS particles size prevent instantaneously uniform T_p, except in case of highly conductive materials such as Al and Cu, or using a very fine particle size of about 1µm for weakly conductive media similar to Al_2O_3 (Table 7). Then, the choice of unit reference for the travel distance decides the reliability of an instantaneousness uniform T_p.

Despite they are less conductive, Ti and Al_2O_3 also produce a convergence of ΔT towards a stable value that is weak for low D_p. The notion of instantaneousness uniform T_p prevails for $\delta x = 1mm$ as supported by the condition $t_p/t_U > 1$ (tables 4-7). These computed ratios t_p/t_U also match with the depiction in (Fig. 5a) and proves thereby the consistency of the analytical condition RUT_p<1 to discuss whether or not there is a suitability of instantaneous uniform T_p. In case of high D_p, ΔT converges later than t_U for any δx in between 1µm-1mm that gives $t_p/t_U \gg 1$. Furthermore, the values of converged ΔT for these high sized Ti and Al_2O_3 particles are higher than the other cases, and persist. This temporal response specifies that large particles with low thermal conductivity fail to produce an instantaneous uniform temperature. These results also support the depiction using the analytical dimensionless parameter RUT_p that suggested an event a circumstance of non-uniform t_p for high sized Ti and Al_2O_3 powders ($RUT_p \approx 1$). The criterion RUT_p is then predictive for several typical experimental cases met in cold spraying.

Gas	Cu D_p(μm)	V_∞(m/s)	T_∞(°C)	t_p (s) for various δx 1μm	10μm	100μm	1000μm	t_U (s)	ΔT (°C)	t_p/t_U for various δx 1μm	10μm	100μm	1000μm
Air	5	300	800	3.5E-08	1.3E-07	5.5E-07	3.1E-06	1.0E-08	6.86	3.5	13	55	310
	50	600		1.0E-07	4.0E-07	1.4E-06	5.6E-06	1.0E-06	5.26	0.1	0.4	1.4	5.6
Helium	5	1200	600	3.7E-08	1.1E-07	4.0E-07	1.9E-06	1.0E-08	2.61	3.7	11	40	190
	50	1800		1.1E-07	3.9E-07	1.2E-06	4.6E-06	1.0E-06	4.18	0.11	0.39	1.2	4.6

Table 4. Computational case for Cu particle: results and comparison between (t_U) and (t_p) for the travelled distance δx.

Gas	Al D_p(μm)	V_∞(m/s)	T_∞(°C)	t_p (s) for various δx 1μm	10μm	100μm	1000μm	t_U (s)	ΔT (°C)	t_p/t_U for various δx 1μm	10μm	100μm	1000μm
Air	1	150	800	1.1E-08	5.0E-08	2.9E-07	2.2E-06	<1E-09	0.23	>11	>50	>290	>2200
	50	300		6.5E-08	2.5E-07	9.0E-07	4.2E-06	2.0E-06	2.57	0.03	0.13	0.5	2.1
Helium	1	800	600	1.0E-08	4.0E-08	1.7E-07	1.2E-07	<1E-09	0.61	>10	>40	>170	>120
	50	1200		8.0E-08	2.5E-07	7.0E-07	3.0E-06	2.0E-06	4.57	0.04	0.13	0.35	2.5

Table 5. Computational case for Al particle: results and comparison between (t_U) and (t_p) for the travelled distance δx.

Gas	Ti D_p(μm)	V_∞(m/s)	T_∞(°C)	t_p (s) for various δx 1μm	10μm	100μm	1000μm	t_U (s)	ΔT (°C)	t_p/t_U for various δx 1μm	10μm	100μm	1000μm
Air	10	350	800	3.5E-08	1.3E-07	5.5E-07	3.1E-06	5.0E-07	7.13	0.07	0.26	1.1	6.2
	50	550		7.0E-08	2.7E-07	1.0E-06	4.6E-06	2.0E-05	14.3	0.004	0.01	0.05	0.2
Helium	10	1300	600	3.7E-08	1.1E-07	4.0E-07	1.9E-06	5.0E-07	12.4	0.07	0.22	0.80	3.8
	50	1600		8.0E-08	2.5E-07	0.8E-06	3.3E-06	2.0E-05	31.4	0.004	0.01	0.04	0.2

Table 6. Computational case for Ti particle: results and comparison between (t_U) and (t_p) for the travelled distance δx.

Gas	Al_2O_3 D_p(μm)	V_∞(m/s)	T_∞(°C)	t_p(s) for various δx 1μm	10μm	100μm	1000μm	t_U (s)	ΔT (°C)	t_p/t_U for various δx 1μm	10μm	100μm	1000μm
Air	1	150	800	1.2E-08	5.5E-08	3.1E-07	1.8E-07	<1E-09	0.01	>12	>55	>310	>18
	50	550		7.0E-08	2.7E-07	1.0E-06	4.6E-06	2.0E-05	12.8	0.004	0.01	0.1	0.2
Helium	1	800	600	1.2E-08	4.5E-08	1.9E-07	1.6E-07	<1E-09	0.01	>12	>45	>190	>16
	50	1600		8.0E-08	2.5E-07	0.8E-06	3.3E-06	2.0E-05	25.9	0.004	0.01	0.04	0.2

Table 7. Computational case for Al_2O_3 particle: results and comparison between (t_U) and (t_p) for the travelled distance δx.

3.3 Conclusive remarks regarding the particle temperature during cold spraying

A thermomechanical softening due to T_p can facilitate the bonding in cold spraying [5,8]. Some experiments have shown improvements of deposition efficiency based on such effect. The softening of the particles were produced by annealing and stress relaxation after a long preheating of the powder feedstock [9,24]. The change in mechanical properties remains permanent until the collision on the substrate. Unlike this preheating solution, heating of the particles by setting the inlet propellant gas at a high temperature is ineffective since the instantaneously uniform T_p follows the decreasing thermal field of the flowing gas due to the expansion inside the nozzle and, more importantly, outside during the atmospheric expansion. Furthermore, the gas cooling is not the sole thermal phenomenon during the expansion. Flow instabilities due to turbulence outside the nozzle, shock waves due to under-expansion or over-expansion, flow stagnation ahead the substrate due to the impinging compressive jet; these are additional phenomena that can involve strong and irregular changes of the gas temperature along the flow direction. Therefore, the particles are subjected to thermal variations that are difficult to control. Using the thermal field of the flowing gas is then tricky to reach a specific value of T_p for the stage of collision onto the substrate. An efficient heating should be able to overcome the fluctuation of the gas temperature during the expansion. The instantaneous response of T_p should be a constant temperature, high enough to promote the thermomechanical softening during the collision. A few studies have suggested a kind of thermal tailoring conducive to such situation. Researchers at University of Ottawa Cold Spray Laboratory have developed an impulse cold spray method, capable of reaching supersonic velocities while the gas remains heated outside the nozzle [25–28]. This method, denoted pulse gas dynamic spraying, uses a propagation of compression waves produced by a cyclic shock impulse that simultaneously accelerates and heat the gas throughout a barrel type nozzle. The compression waves produce a temperature increase at the nozzle exhaust zone and enables thereby a sort of thermal tailoring capable of heating the particles until their collisions onto the substrate. This cold spraying variance enables a successful deposition of thick coatings using hard powders [25] and large variety of materials viz. amorphous compounds, Cermet, nanocrystalline powder, composites; in addition to metals [25–28]. Better homogenization of composite coatings [28], improvement of coating property such as the hardness [27] were also positive effects produced the particles heating using this self-heating cold gas spray method.

For conventional cold spraying, a method that matches with both quickness of the deposition and fast-thermal reactivity of the particles is a non-contact heating by means of laser irradiation. A laser beam acts on the particles with a synchronous motion with the nozzle to ensure a continuous heating during the deposition. Such alternative offers more deposition capability and also improvements of coating features [29–35]. There are two variances of moving heating source depending on the configuration between the particles jet and the laser beam. Some studies exploited a concentric disposition of both laser heating spot and particles jet spot ahead the substrate using a simple oblique disposition of the laser beam near the nozzle [29–31]. Depositions with an angle of 15° have led to expected positive thermal effects [29,35]. A laser heating up to 800°C was generated during the deposition of copper powders that resulted in about two-fold increase in coating thickness and full densification as compared to conventional CGDS method [29]. Yao et al. did succeed in reaching a focused heating up to 1000°C that enabled a strongly bonded diamond/Ni coating with a dense microstructure, non-transformed phases and then increased tribological performances [30]. Similar achievements were also obtained for other metals, that are highly dense titanium coating [31] and corrosion resistant Al-Si coating with a good structural integrity [35]. Improvement of deposition efficiency were also observed [35].

The other disposition of the laser heating is a coaxial configuration between the laser beam and the nozzle using an optical device that reflects the laser source from a beam expander towards the substrate through the nozzle cross-section [32]. Against the concentric oblique configuration, this coaxial disposition can continuously heat the particles along the nozzle axis from the inside to the outside and ahead the substrate until the collision. This method was experienced for the deposition of TiO_2 nanoparticles onto FTO-glass and ITO-PET substrates using micronozzle. The typical potential application is the fabrication of DSSCs (Dye-sensitized solar cells). The laser heating involved a better self-consolidation of the TiO_2 nanoparticles within the coating with a thickening up to 14µm, free of physically and thermally activated defects, and without transformation of the primary anatase nature of TiO_2 particles. These positive thermal effects contribute for better photovoltaic efficiencies [32]. Furthermore, the better structural inter-cohesion thanks to the coaxial laser assistance provides a structural integrity improvement. Increase in elastic modulus and hardness from 1.7GPa to 5GPa and 0.22GPa to 0.31GPa, respectively, was obtained [32]. Together, these examples highlight issues and suitable alternatives related to the instantaneousness of the particle temperature during conventional cold spraying.

4. Conclusions

This paper investigates the transient heat transfer within solid micron powders due to the convective exchange with the gas flow during cold spraying. Conditions of instantaneously uniform temperature are depicted using analytical laws and coupled fluid/solid numerical simulations.

- The analytical solution of the particle's temperature gives a dimensionless criterion for a uniform distribution, denoted RUT_p, depending on the gas velocity over the particle surface, the particle size and the ratio between the thermal conductivities of both particle and gas.
- Representative computed values of RUT_p show that during cold spraying, the temperature field within particles (T_p) is mostly instantaneously uniform.
- CFD simulations of the convective exchange between particle and gas flow assess the duration of the transient heat transfer within particle (t_U) before a quasi-uniform temperature distribution.
- Analytical solution for the particle residence time (t_p) over a travelled distance *dx* enables for discussing the instantaneousness of uniform T_p.
- T_p is not strictly instantaneously uniform since for very short unit of travelled distance such as δx=1µm: $t_p < t_U$.
- The reference distance *dx*=1mm of the literature well produces uniform T_p, that supports the notion of instantaneous T_p which is widely enacted to compute T_p depending on the gas flow using the Newton's law of parietal convection, based on this reference unit δx =1mm.
- The comparison between both durations t_U and t_p also supports the consistency of the analytical condition for RUT_p to discuss whether there is a suitability of instantaneous uniform T_p.
- As conclusive remarks, issues due to the instantaneous variation of T_p during cold spraying are reviewed and discussed with the suitable alternatives for efficiently heating the particles.

Appendix: Details of the analytical calculation of the solution $T_p(r,t)$

The differential equation (Eq. 1) was treated in the heat transfer textbook [36] but under some simplifications that slightly differ from the problem (Eq. 1-3). In [36], a reduction into a one-dimensional formulation in cartesian coordinate is suggested and the analytical resolution relies on a case of linear flow for an infinite plate subjected to zero temperature at one edge and a convection at the opposite edge using a zero ambient temperature. For the sake consistency and accuracy, the boundary condition (Eq. 2) should however be satisfied as it is formulated. A proved analytical solution that meets the whole conditions (Eq .1-3) is then crucial for the study in this paper. Such solution can be established using dimensionless parameters, separation of variables and transformation into an eigenvalue problem. The variables of (Eq. 1-3) are replaced by dimensionless parameters as follows:

$$\begin{cases} \tilde{t} = \dfrac{t}{\tau} \\ \tilde{r} = \dfrac{r}{\frac{Dp}{2}} \\ \tilde{T} = \dfrac{T - T_\infty}{T_0 - T_\infty} \end{cases} \qquad \text{(Eq. A1 -A3)}$$

Where τ is defined as the characteristic time of diffusion:

$$\tau = \frac{\left(\frac{Dp}{2}\right)^2}{\alpha} \qquad \text{(Eq. A4)}$$

where α is the thermal diffusivity.

Then, the problem (Eq. 1-3) becomes:

$$\frac{1}{\tilde{r}^2}\frac{d}{d\tilde{r}}\left[\tilde{r}^2\frac{d\tilde{T}_p(\tilde{r},\tilde{t})}{d\tilde{r}}\right] = \frac{d\tilde{T}_p(\tilde{r},\tilde{t})}{d\tilde{t}} \qquad for \begin{cases} \tilde{r} \in [0,1] \\ \tilde{t} \geq 0 \end{cases} \qquad \text{(Eq. A5)}$$

$$-\frac{d\tilde{T}_p(\tilde{r},\tilde{t})}{d\tilde{r}}\bigg|_{\tilde{r}=1} = Bi\,\tilde{T}_p(1,\tilde{t}\,) \qquad \text{(Eq. A6)}$$

$$\tilde{T}_p(\tilde{r},0\,) = 1 \qquad \text{(Eq. A7)}$$

Where Bi is defined in (Eq. 5)

This problem can be solved by the method of separation of variables. Assuming the solution $\tilde{T}_p(\tilde{r},\tilde{t})$ has the form:

$$\tilde{T}_p(\tilde{r},\tilde{t}\,) = g(\tilde{r})f(\tilde{t}) \qquad \text{(Eq. A8)}$$

and, using these separated variables, (Eq. A5) gives the differential equation:

$$\frac{f\prime(\tilde{t})}{f(\tilde{t})} = \frac{1}{g(\tilde{r})}\left(\frac{2g\prime(\tilde{r})}{\tilde{r}} + g''(\tilde{r})\right) \qquad \text{(Eq. A9)}$$

which can be formulated into an eigenvalue problem using an intermediate parameter denoted ζ. Then, the differential form (Eq. A9) can be dissociated into:

$$\begin{cases} \frac{f'(\tilde{t})}{f(\tilde{t})} = -\zeta^2 \\ \frac{1}{g(\tilde{r})}\left(\frac{2g'(\tilde{r})}{\tilde{r}} + g''(\tilde{r})\right) = -\zeta^2 \end{cases} \quad \text{(Eq. A10-A11)}$$

The differential form (Eq. A10) gives an obvious solution:

$$f_i(\tilde{t}) = Ke^{-\zeta_i^2 \tilde{t}} \quad \text{(Eq. A12)}$$

Where K is a constant of integration.

Using the following rearrangement, we can identify that (Eq. A11) is a differential equation of Sturm-Liouville:

$$g''(\tilde{r}) + \frac{2}{\tilde{r}} g'(\tilde{r}) - \zeta^2 g(\tilde{r}) = 0 \quad \text{(Eq. A13)}$$

whose solution must satisfy the conditions (Eq. A6, A7). Instead of solving (Eq. A13) in this form, we can suggest a formulation of an eigenvalue problem assuming a solution in a form $g(\tilde{r}) = \phi(\tilde{r})/\tilde{r}$. Then, we obtain an ordinary differential form of (Eq. A13):

$$\frac{\phi''(\tilde{r})}{\phi(\tilde{r})} = -\zeta^2 \quad \text{(Eq. A14)}$$

Therefore, using the new form for $g(\tilde{r})$ in (Eq. A5-A7) results in the eigenvalue problem:

$$\begin{cases} \frac{\phi''(\tilde{r})}{\phi(\tilde{r})} = -\zeta^2 \\ -[\phi'(1) - \phi(1)]f(\tilde{t}) = Bi[\phi(1)]f(\tilde{t}) \\ \frac{\phi(\tilde{r})}{\tilde{r}} f(0) = 1 \end{cases} \quad \text{(Eq. A15-A17)}$$

That can be rearranged into:

$$\begin{cases} \phi''(\tilde{r}) + \zeta^2 \phi(\tilde{r}) = 0 \\ \frac{\phi'(1)}{\phi(1)} = 1 - Bi \\ \phi(\tilde{r}) = K^{-1}\tilde{r} \end{cases} \quad \text{(Eq. A18-A20)}$$

that form a case of Sturm-Liouville problem where (Eq. A19, A20) is an eigenvalue problem. The eigenvalues ζ are determined by a transcendental form obtained from (Eq. A19). Basically, the solution of (Eq. A18) for each eigenvalue ζ_i has the form:

$$\phi_i(\tilde{r}) = \mathrm{A}\cos(\zeta_i \tilde{r}) + B\sin(\zeta_i \tilde{r}) \quad \text{(Eq. A21)}$$

Since the solution $\tilde{T}_p(\tilde{r}, \tilde{t})$ is continuous and finite as $\tilde{r} \to 0$, we assume A=0 and seek a solution $\phi(\tilde{r})$ of type $\mathrm{B}\sin(\zeta_i \tilde{r})$. Thus, the boundary condition (Eq. A16) results in the transcendental equation:

$$\frac{\zeta_i}{\tan \zeta_i} = 1 - Bi \quad \text{(Eq. A22)}$$

which gives the eigenfunctions of (Eq. A19) that constitute solutions of the problem (Eq. A18-A20) as follows:

$$\phi_i(\tilde{r}) = \beta_i \sin(\zeta_i \tilde{r}) \quad \text{(Eq. A23)}$$

Using the properties of linear differential equations, the linear combination of the solutions $\phi_i(\tilde{r}, \zeta_i)$ forms the solution of the eigenvalue problem (Eq. A18, A19):

$$\phi(\tilde{r}) = \sum_{i=1}^{n} \beta_i \sin(\zeta_i \tilde{r}) \quad \text{(Eq. A24)}$$

When substituting (Eq. A24) in (Eq. A20) in order to satisfy the initial condition (Eq. A20) we obtain:

$$\sum_{i=1}^{n} \beta_i \sin(\zeta_i \tilde{r}) = K^{-1} \tilde{r} \quad \text{(Eq. A25)}$$

which is a Fourier series description of the term $K^{-1}\tilde{r}$. The coefficient β_i that satisfies this equation is determined in accordance with the theorem of Sturm-Liouville that makes use of the orthogonality property of the eigenfunctions $\sin(\zeta_i \tilde{r})$:

$$\int_{-1}^{1} \sin(\zeta_i \tilde{r}) \sin\left(\zeta_j \tilde{r}\right) d\tilde{r} = \frac{\sin\left(\zeta_i - \zeta_j\right)}{\zeta_i - \zeta_j} - \frac{\sin\left(\zeta_i + \zeta_j\right)}{\zeta_i + \zeta_j} = 0 \quad \text{(for } i \neq j\text{)} \quad \text{(Eq. A26)}$$

This orthogonality is true for the eigenvalues ζ_i and can be verified by computing (Eq. A26). Values for Bi=0.2 are shown in Table A.1 for the first ten eigenvalues. Since then, β_i is a normalized value of the Fourier coefficient of (Eq. A25):

$$\beta_i = \frac{\int_{-1}^{1} K^{-1}\, \tilde{r} \sin(\zeta_i \tilde{r}) d\tilde{r}}{\int_{-1}^{1} \sin^2(\zeta_i \tilde{r}) d\tilde{r}} = K^{-1} \frac{\int_{-1}^{1} \tilde{r} \sin(\zeta_i \tilde{r}) d\tilde{r}}{\int_{-1}^{1} \sin^2(\zeta_i \tilde{r}) d\tilde{r}} \quad \text{(Eq. A27)}$$

That gives:

$$\beta_i = K^{-1} \frac{2}{\zeta_i} \frac{(\sin \zeta_i - \zeta_i \cos \zeta_i)}{(\zeta_i - \sin \zeta_i \cos \zeta_i)} \quad \text{(Eq. A28)}$$

Thus, each solution that corresponds to each eigenvalue is:

$$\tilde{T}_{p_i}(\tilde{r}, \tilde{t}\,) = \frac{\phi_i(\tilde{r})}{\tilde{r}} f_i(\tilde{t}) = \frac{2}{\zeta_i \tilde{r}} \frac{(\sin \zeta_i - \zeta_i \cos \zeta_i)}{(\zeta_i - \sin \zeta_i \cos \zeta_i)} \sin(\zeta_i \tilde{r})\, e^{-\zeta_i^2 \tilde{t}} \quad \text{(Eq. A29)}$$

and the linear combination solution is:

$$\tilde{T}_p(\tilde{r}, \tilde{t}\,) = 2 \sum_{i=1}^{n} \frac{(\sin \zeta_i - \zeta_i \cos \zeta_i)}{(\zeta_i - \sin \zeta_i \cos \zeta_i)} e^{-\zeta_i^2 \tilde{t}} \frac{\sin(\zeta_i \tilde{r})}{\zeta_i \tilde{r}} \quad \text{(Eq. A30)}$$

Finally, when replacing the dimensionless parameters by their definition (Eq. A1 -A3), we obtain the final solution of $T_p(r, t)$.

$$T_p(r,t) = 2(T_0 - T_\infty) \sum_{i=1}^{n} \left[\left\{ \frac{sin\zeta_i - \zeta_i cos\zeta_i}{\zeta_i - sin\zeta_i cos\zeta_i} e^{-{\zeta_i}^2 \frac{\lambda_p \quad 4}{\rho_p C_{pp} D_p^2} t} \right\} \frac{sin\left(\frac{2\zeta_i}{D_p} r\right)}{\frac{2\zeta_i}{D_p} r} \right] + T_0 \quad \text{(Eq. A31)}$$

which can be reduced to the first term ($i = 1$) because the terms $\left\{\theta(\zeta_i) e^{-{\zeta_i}^2 Fo}\right\}$ for ($i \geq 2$) become neglectable over the computed range of the Fourier number Fo (Table A.2). Then, the expression of $T_p(r, t)$ is simplified into (Eq. 4) since the values of Fo lie in between [0.1-10] for the duration (t_U) computed with the typical cold spray data in this paper.

	ζ_i									
ζ_i	0.759	4.538	7.751	10.922	14.080	17.232	20.381	23.528	26.674	29.818
0.759		4.42E-08	1.50E-08	7.54E-09	4.53E-09	3.02E-09	2.16E-09	1.62E-09	1.26E-09	1.01E-09
4.538	4.42E-08		1.49E-11	6.31E-16	2.50E-13	1.09E-16	1.96E-16	1.67E-16	6.02E-12	1.59E-16
7.751	1.50E-08	1.49E-11		1.01E-11	4.00E-12	2.52E-12	1.68E-12	1.21E-12	5.53E-12	7.21E-13
10.922	7.54E-09	6.31E-16	1.01E-11		5.69E-13	6.07E-17	4.42E-17	3.17E-16	7.11E-12	8.24E-18
14.080	4.53E-09	2.50E-13	4.00E-12	5.69E-13		4.56E-13	2.07E-13	1.27E-13	8.13E-12	6.50E-14
17.232	3.02E-09	1.09E-16	2.52E-12	6.07E-17	4.56E-13		1.14E-16	5.82E-16	1.02E-11	1.21E-16
20.381	2.16E-09	1.96E-16	1.68E-12	4.42E-17	2.07E-13	1.14E-16		9.02E-16	1.43E-11	2.27E-16
23.528	1.62E-09	1.67E-16	1.21E-12	3.17E-16	1.27E-13	5.82E-16	9.02E-16		2.67E-11	6.59E-16
26.674	1.26E-09	6.02E-12	5.53E-12	7.11E-12	8.13E-12	1.02E-11	1.43E-11	2.67E-11		2.38E-11
29.818	1.01E-09	1.59E-16	7.21E-13	8.24E-18	6.50E-14	1.21E-16	2.27E-16	6.59E-16	2.38E-11	

Table A1. Verification of the orthogonality property of the eigenfunctions $\sin(\zeta_i \tilde{r})$: values (Eq. A28) in term of absolute value using Bi=0.2 over the first ten eigenvalues.

	ζ_i									
Fo	0.759	4.538	7.751	10.922	14.080	17.232	20.381	23.528	26.674	29.818
0.1	5.0E-01	5.8E-03	6.4E-05	1.2E-07	3.5E-11	1.5E-15	9.0E-21	7.7E-27	9.4651E-34	1.6E-41
1	3.0E-01	5.1E-11	2.1E-28	2.8E-54	1.1E-88	1.3E-131	3.9E-183	3.3E-243	7.6E-312	0
10	1.7E-03	1.7E-91	3.1E-263	0	0	0	0	0	0	0

Table A2. Computed values of $\left\{\theta(\zeta_i)e^{-{\zeta_i}^2 Fo}\right\}$ (in terms on absolute value) that enables for reducing the expression of $T_p(r,t)$ to the first term of (Eq. A33).

Fo	$\tilde{T}_c$	Fo	$\tilde{T}_c$	Fo	$\tilde{T}_c$	Fo	$\tilde{T}_c$	Fo	$\tilde{T}_c$
0	1	0.15	0.830	0.31	0.560	0.46	0.360	0.62	0.230
0.01	1	0.17	0.810	0.32	0.530	0.48	0.350	0.63	0.220
0.03	1	0.18	0.770	0.33	0.510	0.5	0.340	0.65	0.215
0.04	0.990	0.2	0.740	0.35	0.500	0.51	0.320	0.67	0.210
0.06	0.980	0.22	0.710	0.37	0.480	0.53	0.310	0.68	0.200
0.07	0.970	0.23	0.680	0.38	0.450	0.54	0.290	0.70	0.190
0.09	0.940	0.24	0.660	0.4	0.430	0.56	0.280		
0.1	0.930	0.26	0.630	0.42	0.410	0.57	0.275		
0.12	0.880	0.28	0.610	0.43	0.400	0.59	0.250		
0.14	0.860	0.29	0.580	0.44	0.380	0.61	0.240		

Table A3. Experimental data obtained from the literature case of a forced-air cooling over a spherical medial [23].

Fo	$\tilde{T}_c$	Fo	$\tilde{T}_c$	Fo	$\tilde{T}_c$	Fo	$\tilde{T}_c$	Fo	$\tilde{T}_c$	Fo	$\tilde{T}_c$
0	0.992	0.12	0.849	0.24	0.611	0.37	0.437	0.49	0.313	0.61	0.224
0.01	0.990	0.13	0.823	0.26	0.591	0.38	0.423	0.50	0.303	0.62	0.217
0.02	0.997	0.15	0.797	0.27	0.571	0.39	0.409	0.51	0.293	0.64	0.210
0.04	0.996	0.16	0.772	0.28	0.552	0.40	0.396	0.53	0.283	0.65	0.203
0.05	0.984	0.17	0.747	0.29	0.534	0.42	0.383	0.54	0.274	0.66	0.196
0.06	0.969	0.18	0.722	0.31	0.516	0.43	0.370	0.55	0.265	0.67	0.190
0.07	0.948	0.20	0.699	0.32	0.499	0.44	0.358	0.56	0.256	0.68	0.184
0.09	0.926	0.21	0.675	0.33	0.483	0.45	0.346	0.57	0.248	0.70	0.178
0.10	0.901	0.22	0.653	0.34	0.467	0.46	0.335	0.59	0.240		
0.11	0.875	0.23	0.632	0.35	0.452	0.48	0.324	0.60	0.232		

Table A4. Numerical data obtained from the computational model described in section 2.3 and applied to the literature case of Table A3 [23].

References

[1] R.N. Raoelison, Ch. Verdy, H. Liao, Cold gas dynamic spray additive manufacturing today: Deposit possibilities, technological solutions and viable applications, Mater. Des. 133 (2017) 266–287. https://doi.org/10.1016/j.matdes.2017.07.067.

[2] R.N. Raoelison, Coeval Cold Spray Additive Manufacturing Variances and Innovative Contributions, in: Cold-Spray Coat., Springer, Cham, 2018: pp. 57–94. https://doi.org/10.1007/978-3-319-67183-3_3.

[3] A. Moridi, S.M. Hassani-Gangaraj, M. Guagliano, M. Dao, Cold spray coating: review of material systems and future perspectives, Surf. Eng. 30 (2014) 369–395.

[4] H. Assadi, H. Kreye, F. Gärtner, T. Klassen, Cold spraying – A materials perspective, Acta Mater. (n.d.). https://doi.org/10.1016/j.actamat.2016.06.034.

[5] T. Schmidt, F. Gärtner, H. Assadi, H. Kreye, Development of a generalized parameter window for cold spray deposition, Acta Mater. 54 (2006) 729–742. https://doi.org/10.1016/j.actamat.2005.10.005.

[6] H. Assadi, T. Schmidt, H. Richter, J.-O. Kliemann, K. Binder, F. Gärtner, T. Klassen, H. Kreye, On Parameter Selection in Cold Spraying, J. Therm. Spray Technol. 20 (2011) 1161–1176. https://doi.org/10.1007/s11666-011-9662-9.

[7] H. Assadi, F. Gärtner, T. Stoltenhoff, H. Kreye, Bonding mechanism in cold gas spraying, Acta Mater. 51 (2003) 4379–4394. https://doi.org/10.1016/S1359-6454(03)00274-X.

[8] T. Schmidt, H. Assadi, F. Gärtner, H. Richter, T. Stoltenhoff, H. Kreye, T. Klassen, From Particle Acceleration to Impact and Bonding in Cold Spraying, J. Therm. Spray Technol. 18 (2009) 794–808. https://doi.org/10.1007/s11666-009-9357-7.

[9] X.-J. Ning, J.-H. Jang, H.-J. Kim, The effects of powder properties on in-flight particle velocity and deposition process during low pressure cold spray process, Appl. Surf. Sci. 253 (2007) 7449–7455. https://doi.org/10.1016/j.apsusc.2007.03.031.

[10] K.H. Ko, J.O. Choi, H. Lee, Pretreatment effect of Cu feedstock on cold-sprayed coatings, J. Mater. Process. Technol. 214 (2014) 1530–1535. https://doi.org/10.1016/j.jmatprotec.2014.02.020.

[11] Y. Xie, M.-P. Planche, R. Raoelison, P. Hervé, X. Suo, P. He, H. Liao, Investigation on the influence of particle preheating temperature on bonding of cold-sprayed nickel coatings, Surf. Coat. Technol. (n.d.). https://doi.org/10.1016/j.surfcoat.2016.09.037.

[12] S. Yin, M. Meyer, W. Li, H. Liao, R. Lupoi, Gas Flow, Particle Acceleration, and Heat Transfer in Cold Spray: A review, J. Therm. Spray Technol. 25 (2016) 874–896. https://doi.org/10.1007/s11666-016-0406-8.

[13] M. Hassani-Gangaraj, D. Veysset, K.A. Nelson, C.A. Schuh, In-situ observations of single micro-particle impact bonding, Scr. Mater. 145 (2018) 9–13. https://doi.org/10.1016/j.scriptamat.2017.09.042.

[14] M. Hassani-Gangaraj, D. Veysset, K.A. Nelson, C.A. Schuh, Impact-Bonding with Aluminum, Silver, and Gold Microparticles: Toward Understanding the Role of Native Oxide Layer, Appl. Surf. Sci. (2019). https://doi.org/10.1016/j.apsusc.2019.01.111.

[15] R.N. Raoelison, Y. Xie, T. Sapanathan, M.P. Planche, R. Kromer, S. Costil, C. Langlade, Cold gas dynamic spray technology: A comprehensive review of processing conditions for various technological developments till to date, Addit. Manuf. 19 (2018) 134–159. https://doi.org/10.1016/j.addma.2017.07.001.

[16] H. Katanoda, Numerical Simulation of Temperature Uniformity within Solid Particles in Cold Spray, J. Solid Mech. Mater. Eng. 2 (2008) 58–69. https://doi.org/10.1299/jmmp.2.58.

[17] R.N. Raoelison, Analytical description of solid particles kinematics due to a fluid flow and application to the depiction of characteristic kinematics in cold spraying, Powder Technol. 319 (2017) 191–203. https://doi.org/10.1016/j.powtec.2017.06.029.

[18] F. Chapeau-Blondeau, A. Monir, Numerical evaluation of the Lambert W function and application to generation of generalized Gaussian noise with exponent 1/2, IEEE Trans. Signal Process. 50 (2002) 2160–2165. https://doi.org/10.1109/TSP.2002.801912.
[19] J. Holman, Heat Transfer, 10 edition, McGraw Hill Education, Boston, 2009.
[20] S. Taneda, Experimental Investigation of the Wake behind a Sphere at Low Reynolds Numbers, J. Phys. Soc. Jpn. 11 (1956) 1104–1108. https://doi.org/10.1143/JPSJ.11.1104.
[21] H. Sakamoto, H. Haniu, A study on vortex shedding from spheres in a uniform flow, ASME Trans. J. Fluids Eng. 112 (1990) 386–392.
[22] E. Achenbach, Vortex shedding from spheres, J. Fluid Mech. 62 (1974) 209–221. https://doi.org/10.1017/S0022112074000644.
[23] I. Dincer, Simplified solution for temperature distributions of spherical and cylindrical products during rapid air cooling, Energy Convers. Manag. 36 (1995) 1175–1184. https://doi.org/10.1016/0196-8904(95)00011-2.
[24] K.H. Ko, J.O. Choi, H. Lee, Pretreatment effect of Cu feedstock on cold-sprayed coatings, J. Mater. Process. Technol. 214 (2014) 1530–1535. https://doi.org/10.1016/j.jmatprotec.2014.02.020.
[25] B. Jodoin, P. Richer, G. Bérubé, L. Ajdelsztajn, A. Erdi-Betchi, M. Yandouzi, Pulsed-Gas Dynamic Spraying: Process analysis, development and selected coating examples, Surf. Coat. Technol. 201 (2007) 7544–7551. https://doi.org/10.1016/j.surfcoat.2007.02.033.
[26] E. Sansoucy, P. Marcoux, L. Ajdelsztajn, B. Jodoin, Properties of SiC-reinforced aluminum alloy coatings produced by the cold gas dynamic spraying process, Surf. Coat. Technol. 202 (2008) 3988–3996. https://doi.org/10.1016/j.surfcoat.2008.02.017.
[27] M. Yandouzi, E. Sansoucy, L. Ajdelsztajn, B. Jodoin, WC-based cermet coatings produced by cold gas dynamic and pulsed gas dynamic spraying processes, Surf. Coat. Technol. 202 (2007) 382–390. https://doi.org/10.1016/j.surfcoat.2007.05.095.
[28] M. Yandouzi, P. Richer, B. Jodoin, SiC particulate reinforced Al–12Si alloy composite coatings produced by the pulsed gas dynamic spray process: Microstructure and properties, Surf. Coat. Technol. 203 (2009) 3260–3270. https://doi.org/10.1016/j.surfcoat.2009.04.001.
[29] M. Kulmala, P. Vuoristo, Influence of process conditions in laser-assisted low-pressure cold spraying, Surf. Coat. Technol. 202 (2008) 4503–4508. https://doi.org/10.1016/j.surfcoat.2008.04.034.
[30] J. Yao, L. Yang, B. Li, Z. Li, Beneficial effects of laser irradiation on the deposition process of diamond/Ni60 composite coating with cold spray, Appl. Surf. Sci. 330 (2015) 300–308. https://doi.org/10.1016/j.apsusc.2015.01.029.
[31] M. Bray, A. Cockburn, W. O'Neill, The Laser-assisted Cold Spray process and deposit characterisation, Surf. Coat. Technol. 203 (2009) 2851–2857. https://doi.org/10.1016/j.surfcoat.2009.02.135.
[32] S.-H. Ahn, J.-O. Choi, C.-S. Kim, G.-Y. Lee, H.-T. Lee, K. Cho, D.-M. Chun, C.S. Lee, Laser-assisted nano particle deposition system and its application for dye sensitized solar cell fabrication, CIRP Ann. - Manuf. Technol. 61 (2012) 575–578. https://doi.org/10.1016/j.cirp.2012.03.094.
[33] D.K. Christoulis, M. Jeandin, E. Irissou, J.-G.L. and W. Knapp, Laser-Assisted Cold Spray (LACS), InTech, 2012. http://www.intechopen.com/books/nd-yag-laser/laser-assisted-cold-spray-lacs- (accessed November 8, 2016).
[34] E.O. Olakanmi, Optimization of the Quality Characteristics of Laser-Assisted Cold-Sprayed (LACS) Aluminum Coatings with Taguchi Design of Experiments (DOE), Mater. Manuf. Process. 31 (2016) 1490–1499. https://doi.org/10.1080/10426914.2014.984306.
[35] E.O. Olakanmi, M. Tlotleng, C. Meacock, S. Pityana, M. Doyoyo, Deposition Mechanism and Microstructure of Laser-Assisted Cold-Sprayed (LACS) Al-12 wt.%Si Coatings: Effects of Laser Power, JOM. 65 (2013) 776–783. https://doi.org/10.1007/s11837-013-0611-6.
[36] H.S. Carslaw, J.C. Jaeger, Conduction of heat in solids, Clarendon Press, 1959.